ACS NANO

www.acsnano.org

ARTICLE

Direct Visualization of Electric-Field-Induced Structural Dynamics in Monolayer Transition Metal Dichalcogenides

Akshay A. Murthy, Teodor K. Stanev, Roberto dos Reis, Shiqiang Hao, Christopher Wolverton, Nathaniel P. Stern, and Vinayak P. Dravid*

Cite This: *ACS Nano* 2020, 14, 1569−1576

Read Online

ACCESS | Metrics & More | Article Recommendations | Supporting Information

ABSTRACT: **Layered transition metal dichalcogenides offer many attractive features for next-generation low-dimensional device geometries. Due to the practical and fabrication challenges related to *in situ* methods, the atomistic dynamics that give rise to realizable macroscopic device properties are often unclear. In this study, *in situ* transmission electron microscopy techniques are utilized in order to understand the structural dynamics at play, especially at interfaces and defects, in the prototypical film of monolayer MoS_2 under electrical bias. Through our sample fabrication process, we clearly identify the presence of mass transport in the presence of a lateral electric field. In particular, we observe that the voids present at grain boundaries combine to induce structural deformation. The electric field mediates a net vacancy flux from the grain boundary interior to the exposed surface edge sites that leaves molybdenum clusters in its wake. Following the initial biasing cycles, however, the mass flow is largely diminished and the resultant structure remains stable over repeated biasing. We believe insights from this work can help explain observations of nonuniform heating and preferential oxidation at grain boundary sites in these materials.**

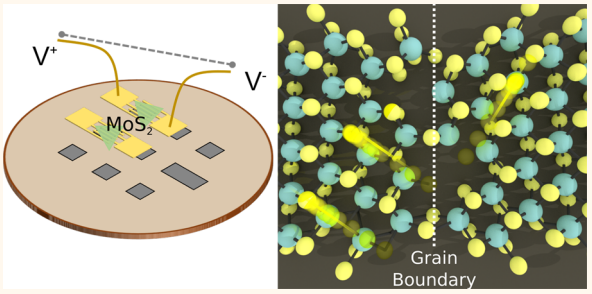

KEYWORDS: *in situ electron microscopy, transition metal dichalcogenides, grain boundaries, MoS_2, electrical transport*

In recent years, defect engineering of layered transition metal dichalcogenides (TMDs) has served as a popular paradigm for constructing unique devices with enhanced functionalities. In particular, point and line defects serve as an effective pathway for tuning the electronic,[1,2] optical,[3,4] and catalytic properties[5,6] in these materials. For example, grain boundaries in TMDs formed through vapor phase synthesis demonstrate electronic properties that differ from the surrounding regions,[7,8] as well as electronic structures that can be modulated by systematically varying the grain boundary tilt angle.[9,10] These interfaces have been used in devices that demonstrate electroluminescent behavior,[11] as well as gate-tunable memristive behavior, making them candidate systems for neuromorphic computation.[12,13] Recent reports, however, have indicated that TMD grain boundaries serve as sites for preferential heating and oxidation during device operation.[14−16] To date, these phenomena have been generally attributed to the presence of nanoporous regions[14] and sulfur vacancies,[15,16] but dynamic high-resolution techniques are essential in order to fully correlate these structures to observable properties.

To better explore these relationships, one particularly useful methodology is *in situ* electrical biasing transmission electron microscopy (TEM). Through this approach, the electrical response of the material can be effectively monitored and correlated directly to nanophysical phenomena. As such, this methodology has achieved significant popularity through electrochemical studies aiming to understand structural dynamics at the electrode interfaces,[17−19] as well as investigations focused on acquiring a mechanistic understanding of electronically induced resistive switching.[20−22] Nonetheless, due to the practical challenges linked to directly probing atomically thin materials using traditional *in situ* biasing sample methods, there have only been a couple of reports investigating monolayer TMDs using this approach.[23,24]

In this study, we develop a fabrication methodology that combines electrical biasing with transmission electron microscopy. This approach allows us to investigate the structural

Received: August 19, 2019
Accepted: January 31, 2020
Published: January 31, 2020

https://dx.doi.org/10.1021/acsnano.9b06581
ACS Nano 2020, 14, 1569−1576

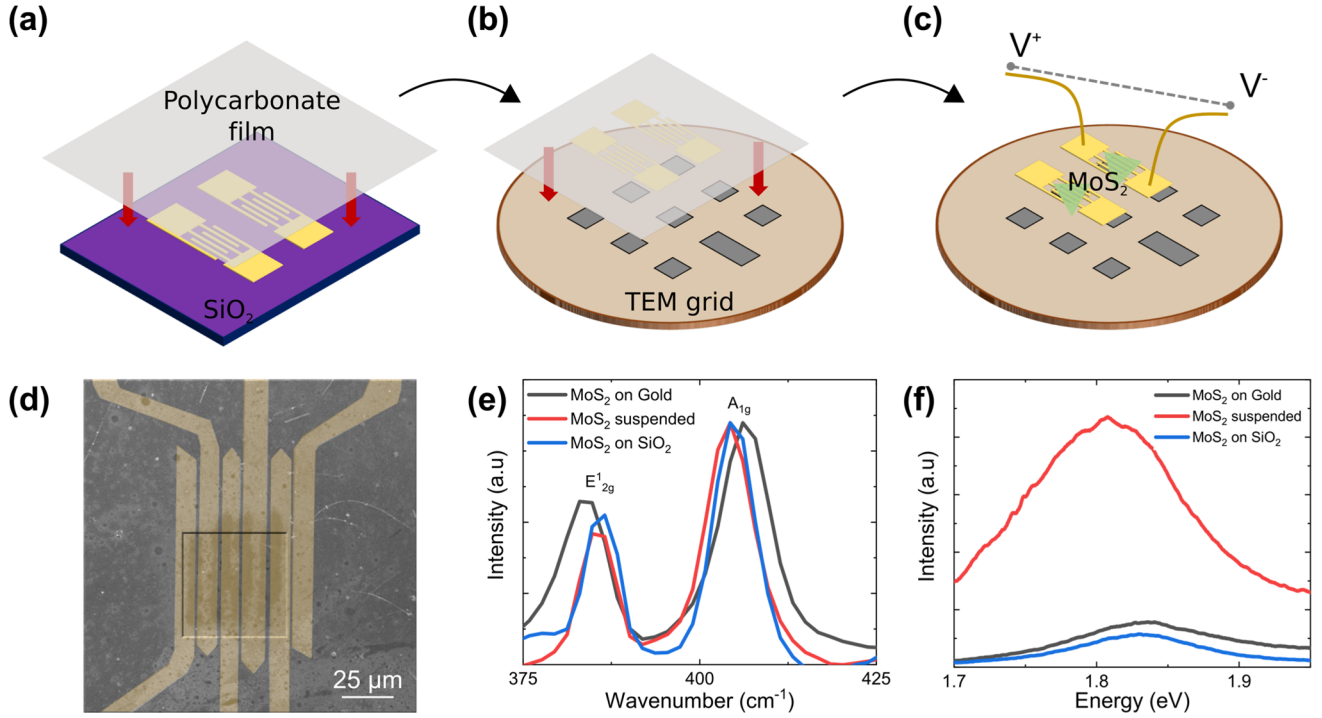

Figure 1. TEM device fabrication. (a–c) Schematic of the fabrication process. Metal electrodes are first picked up from an arbitrary substrate using a polymer support film (a). These electrodes are then placed on a TEM grid (b). Polycrystalline monolayer MoS_2 film is then picked up and placed in an identical fashion (c). (d) Colorized SEM image of fabricated device. The gold color is indicative of the metal electrodes, and the beveled region is indicative of the region where MoS_2 is suspended. As polycrystalline MoS_2 is used, multiple grain boundaries are present in the regions between the electrodes. (e) Raman spectra taken from MoS_2 regions supported on SiO_2, supported on gold, and that are suspended. Due to differences in charge doping and strain between these regions, the positions of the Raman modes vary with substrate. (f) Photoluminescence spectra taken from the same MoS_2 regions. Similarly, due to the inherent differences in charge doping and strain, the position and magnitude of the PL peaks also vary with substrate.

dynamics at play when polycrystalline films of monolayer MoS_2 are electrically biased. We find that when an electric field is applied, strained regions around the grain boundary act as vacancy sources and voids at the grain boundary act as vacancy sinks, leading to a net vacancy flux toward the grain boundaries. Additionally, we find that this vacancy flow process appears to yield regions of molybdenum clusters that aggregate near the voids. Finally, we find that the vacancy flow process does not continue indefinitely, but rather after a few initial biasing cycles, the material reaches a stable state. Assessment of polycrystalline MoS_2 using *in situ* electrical biasing TEM gives the ability to draw direct insights that help us explain the origin of preferential localized heating and oxidation at grain boundary regions that have been demonstrated previously.

RESULTS AND DISCUSSION

In order to prepare a TEM sample for *in situ* electrical biasing, 75 nm gold interdigitated electrodes with a 1 μm spacing are defined on a 300 nm SiO_2/Si substrate. Using a polycarbonate transfer technique described previously,[25] the electrodes were picked up and placed onto a SiO_2/Si TEM grid such that they covered a predefined aperture and created an interdigitated material support bridge (Figure 1a). Subsequently, a polycrystalline film of monolayer MoS_2, synthesized through vapor phase techniques as described in previous reports,[14,26] is then picked up and stacked on top of the gold electrodes using the same polycarbonate stamp technique (Figure 1b). This method allows for monolayer MoS_2 to be suspended between adjacent pairs of electrodes. Finally, wires are bonded between the contact pads and the TEM mount contact points on a Nanofactory holder (Figure 1c). This approach thus allows for applying lateral electric fields across each pair of interdigitated electrodes. A scanning electron microscopy (SEM) image of the interdigitated electrodes and MoS_2 stack is seen in Figure 1d.

A comparison of the Raman and photoluminescence (PL) spectra taken from three distinct regions is provided in Figure 1e,f, respectively. These include spectra taken from the region where MoS_2 is supported by SiO_2 around the aperture, a region where MoS_2 is supported by the gold electrodes, and a region where MoS_2 is suspended. Relative to the suspended region (E^1_{2g} = 384.8 cm^{-1}), the E^1_{2g} mode is red-shifted when MoS_2 is supported by SiO_2 (E^1_{2g} = 386.6 cm^{-1}) and blue-shifted when MoS_2 is supported by the gold electrodes (E^1_{2g} = 383.0 cm^{-1}). With respect to the out-of-plane Raman mode, relative to the suspended region (A_{1g} = 404.3 cm^{-1}), the A_{1g} mode is red-shifted when MoS_2 is supported by the gold electrodes (A_{1g} = 406.1 cm^{-1}), and no discernible change is observed when the MoS_2 is supported by SiO_2 (A_{1g} = 404.3 cm^{-1}). Based on the framework we developed previously to correlate the position of Raman modes to biaxial strain and charge doping in MoS_2,[26] this observation suggests that the MoS_2 supported by the gold electrodes displays the greatest degree of biaxial strain followed by the suspended MoS_2 and then the MoS_2 supported by the SiO_2 region. The biaxial strain measured in the MoS_2 layer supported by gold can likely be attributed to the strong interactions between gold and sulfur atoms.[27] In particular, because gold and MoS_2 have a large lattice mismatch,[28] these strong interfacial interactions likely induce strain in the monolayer MoS_2. Additionally, the moderate level of biaxial

https://dx.doi.org/10.1021/acsnano.9b06581
ACS Nano 2020, 14, 1569–1576

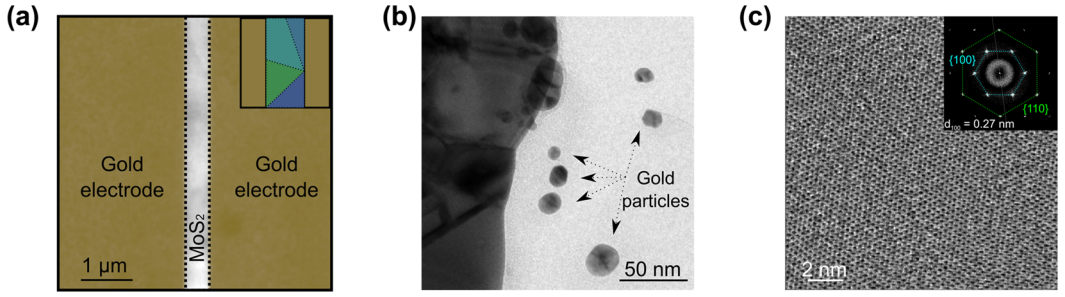

Figure 2. TEM analysis of MoS_2. (a) Low-magnification TEM image of suspended material. Gold region corresponds to metal electrodes, and the area between dotted lines represents MoS_2. Inset provides a schematic representation of the region. In this inset, gold once again corresponds to the electrodes, whereas the different hues of blue are indicative of MoS_2 grains with different orientations, and multiple grain boundaries are present. (b) Low-magnification TEM image of the electrode (left)/MoS_2 (right) interface. Gold nanoparticles are found to be embedded in the MoS_2 matrix. (c) High-resolution TEM image of the MoS_2 region with a corresponding FFT provided as an inset.

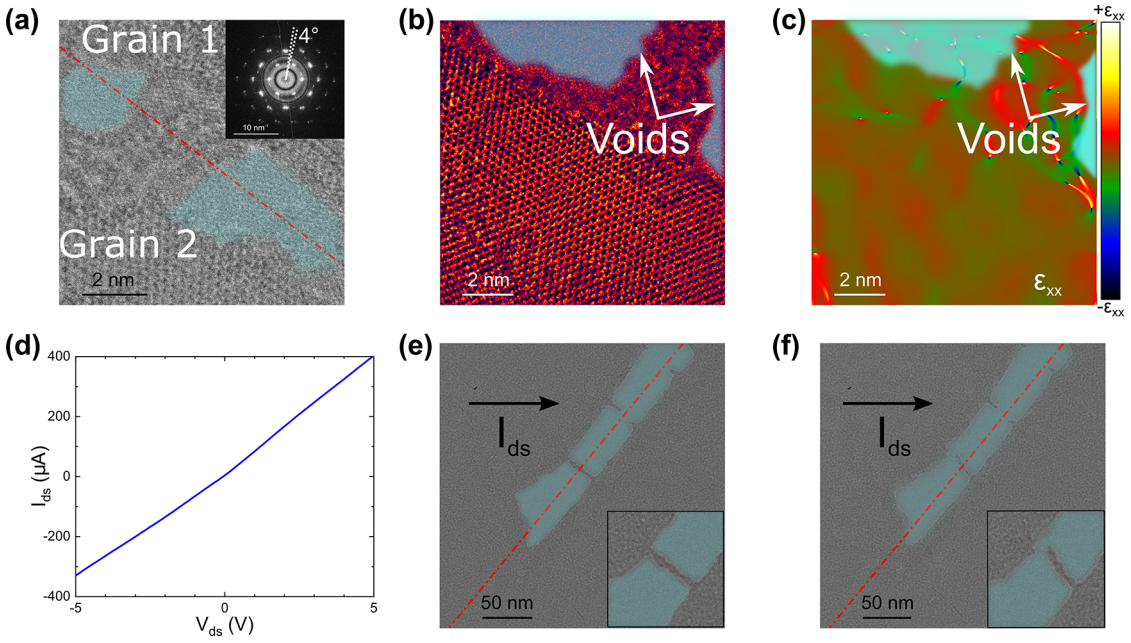

Figure 3. *In situ* biasing across MoS_2 grain boundary. Grain boundaries are indicated with a red dotted line, and voids are colored in blue in all TEM images to aid the eye. (a) High-resolution TEM image of MoS_2 grain boundary with FFT pattern is provided as an inset. A misorientation angle of 4° is measured. FFT patterns for the individual grains are provided in Figure S4. (b) Higher magnification of a void/nanoribbon interface is seen. (c) Normal strain in *x*-direction (ε_{xx}) map of grain boundary region in (b). Strain is highly concentrated near the voids. Additional strain maps for this region are provided in Figure S5. (d) Current−voltage response for the TEM device. Linearity is indicative of quality contacts. (e) Narrow ribbons of material holding together two grains separated by voids prior to biasing. Narrow ribbon of interest is clearly indicated within the inset. (f) Same region following biasing. The narrow ribbon holding together adjacent grains appears to rupture when 1 V is applied across the electrodes, as apparent through the inset. Direction of current (I_{ds}) is indicated.

strain calculated in the suspended region can be attributed to inevitable sinking of the free-standing monolayer in the unsupported region,[29,30] whereas the minimal biaxial strain in the MoS_2 supported by the SiO_2 can be explained by the minimal interlayer interactions observed between transferred monolayer TMDs and amorphous substrates.[26] Similarly, the previously developed framework also indicates that MoS_2 supported by the gold electrodes displays the greatest degree of charge doping followed by MoS_2 supported by the SiO_2 region and then suspended MoS_2. This is also to be expected as gold and SiO_2 substrates have been previously demonstrated to readily dope MoS_2.[26,31] Finally, as shown previously, suspended regions of MoS_2 exhibit significantly greater photoluminescence intensities compared to that of supported regions on SiO_2 or gold.[32] The broad emission from the suspended material can be explained by a combination of moderate strain levels and reduced charge doping in this region.[26]

Low-magnification and high-resolution transmission electron microscopy images of the materials prior to electrical biasing are seen in Figure 2a−c. A fast Fourier transform (FFT) from Figure 2c is provided as the inset and depicts the six-fold symmetry and the expected lattice spacings for MoS_2. These images were taken using a Gatan K3-IS direct electron detector, which allows for imaging of the lattice using a reduced electron total dose on the order of 350 $e^-/Å^2$. Though a slight degree of hydrocarbon accumulation is seen from the diffuse ring in the FFT pattern, this low dose allows for *in situ* imaging of sensitive materials without inducing significant buildup of hydrocarbon residue and/or introducing structural artifacts.

From the representative low-magnification TEM images (Figure 2b), we also observe significant migration of nano-

https://dx.doi.org/10.1021/acsnano.9b06581
ACS Nano 2020, 14, 1569−1576

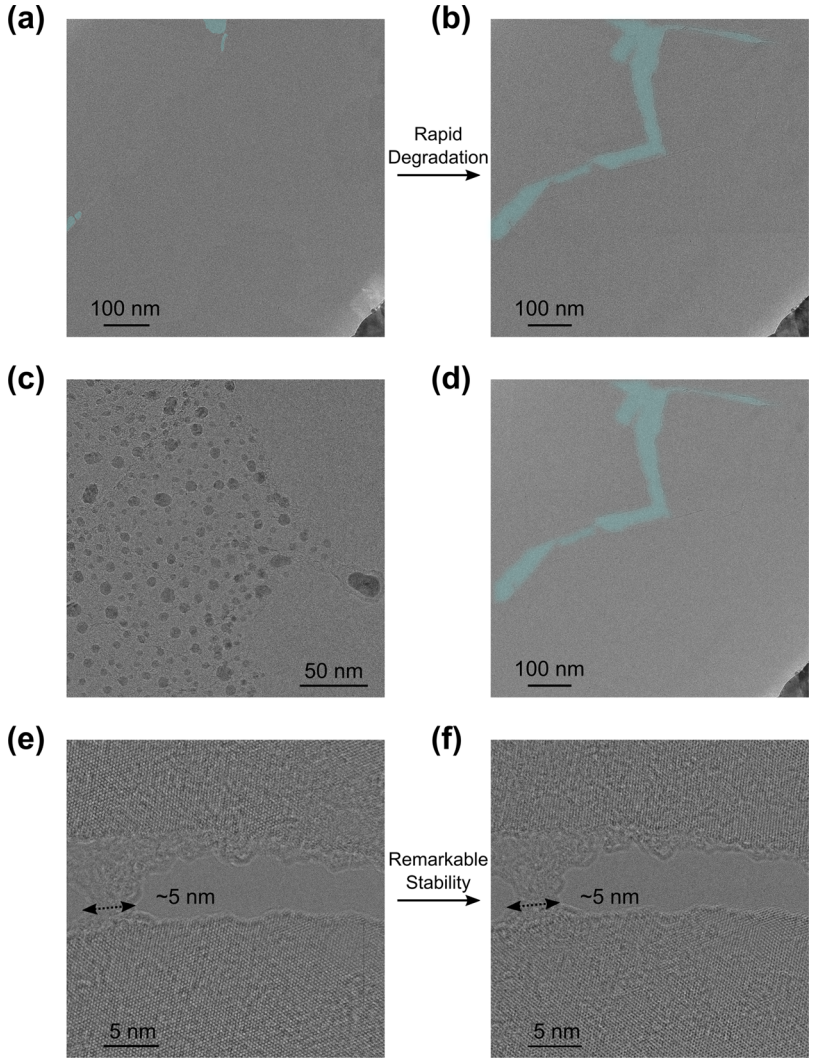

Figure 4. Void coalescence and stabilization. (a) Low-magnification TEM of MoS_2 grain boundary region prior to biasing. Voids are colored in blue to aid the eye. (b) Same region after an electrical bias is applied. As is apparent, neighboring voids (blue) appear to coalesce to form porous chains. (c) After this bias is applied, a number of clusters form within the MoS_2 matrix. After a few biasing cycles, applying an electrical bias does not induce a discernible change in the lattice of MoS_2. (d) Same region in (a) and (b), but the structure largely remains the same after another 5 V bias is applied. (e) High-resolution TEM image of a nanoribbon connecting adjacent to two voids after a few biasing cycles. (f) Same region in (e) after a bias of 10 V is applied. Once more, no discernible changes in structure are evident, and the ribbon retains a lateral dimension of 5 nm.

particles up to 100 nm from the contact−material interface. The chemical and structural nature of these gold particles is confirmed through a selected area electron diffraction pattern provided in Figure S2. Density functional theory (DFT) calculations (Figure S3) suggest that this observation is a result of a low migration energy barrier (0.1 eV) for gold atoms on MoS_2, which is comparable with the diffusion energy barrier predicted for Li ions on MoS_2.[33] This favorable diffusion process is mediated through hopping along adatom sites and likely originates from annealing of the MoS_2−gold electrode TEM structure at 200 °C prior to electrical testing. The observation of this aspect in every device examined in this study is significant for field-effect transistor MoS_2 geometries as it highlights the atomistic dynamics occurring at the metal electrode/MoS_2 interface that need to be considered during electronic measurements. Namely, the potential for migration of gold atoms into MoS_2 suggests a complicated environment at the near-electrode interface where gold nanoparticles can act as vehicles for plasmonic enhancement,[34,35] charge depletion regions,[36] and localized strain in monolayer MoS_2.[37] As such, the perturbations that these gold nanoparticles induce on the local electronic structure[31] may lead to interfacial Coulomb scattering of charge carriers.[38] This aspect would play a major role in short-channel, ballistic-length measurements and can potentially help explain reduced mobilities and conductivities in the sub-200 nm channel length regime.[39]

Additionally, a high-resolution image of a grain boundary is seen in Figure 3a,b. The boundary is indicated by the dotted line, and a tilt angle of 4° is apparent through the accompanying FFT. At this grain boundary region, we see the presence of multiple voids. This feature has been observed previously[14,40,41] and has been attributed to the buildup of stress near a grain boundary. This aspect is supported by geometric phase analysis[42] of this grain boundary region, which indicates that, indeed, strain is primarily concentrated at the grain boundary interface in the vicinity of the voids (Figure 3c and Figure S5). As such, our results agree with the previous strain analysis conducted by Elibol *et al.*, who used the Peierls−Nabarro and the Foreman dislocation models[40] to indicate that void formation at grain

https://dx.doi.org/10.1021/acsnano.9b06581
ACS Nano 2020, 14, 1569−1576

boundaries results from stress release in regions with a large density of dislocation cores.

Although TMD grain boundaries have been explored heavily for functional electronics and optoelectronics,[11−13] the role these voids play during electrical biasing has not been investigated in detail, despite the fact that the presence of these voids reduces the cross-sectional area for electron conduction. As such, the narrow ribbons of material between adjacent voids are expected to exhibit larger current densities and, in turn, appreciable temperature increases.[14] To explore this aspect, an electrical bias of 1 V is applied across adjacent electrodes and the stability of a narrow ribbon with neighboring voids is examined. This electrical potential corresponds to an electric field strength of 1×10^3 V/cm and is well within the voltage range used for standard device operation.[14] The $I-V$ response for this sample is provided in Figure 3d. A linear response is indicative of a small contact resistance, which has been previously shown to be the case when TMDs are transferred onto existing metal electrodes due to the formation of a van der Waals interface largely free of chemical disorder.[43] As is apparent in Figure 3e,f, the application of this electrical potential causes the ribbon to rupture, which suggests that large current densities through these ribbons can be destructive and undesirable (see captured video of this process in SI Video 1). This type of mechanical failure is observed in various regions across the sample, including Figure S6a, and was only observed when a bias was applied across the sample.

In order to better understand the role pre-existing voids play during electrical transport, low-magnification images taken from the grain boundary region are seen in Figure 4a,b. An image taken from the region prior to applying an electrical potential is seen in Figure 4a, where the voids are indicated in blue. Following an applied potential of 5 V across the electrodes, the low-magnification image in Figure 4b demonstrates the significant structural change that this region has undergone. Namely, neighboring nanoscale voids appear to have coalesced to form a large crack on the order of a micron. This behavior is seen in multiple regions across various samples, as is apparent from Figure S6.

In order to better understand the atomistic dynamics at play when an electrical bias is applied across a grain boundary requires examining the migration energy barriers that molybdenum and sulfur atoms face. Understanding the energetics for this type of process is essential because void growth requires migration of both sulfur and molybdenum atoms from the edges of the void to the interior of the grains. As previous DFT calculations indicate,[44,45] intrinsic line defects present in chemical vapor deposition (CVD)-grown MoS_2 offer a low-energy pathway for migration of molybdenum and sulfur atoms. The energy barrier for diffusion through this mode for molybdenum and sulfur atoms is roughly 1.6 eV and between 0.6 and 0.7 eV, respectively. As such, both of these low-energy processes are quite accessible when an electric field is applied across the sample. In addition, based on these calculated energy barriers, it is expected that the migration of sulfur atoms from the edges of the void to the interior of the grain *via* line defects would occur more rapidly than a similar process for molybdenum atoms and thus leave behind a molybdenum-rich region near the void region.

To this end, the representative low-magnification TEM image in Figure 4c demonstrates the presence of numerous clusters residing near the void region. Energy-dispersive spectroscopy confirms the presence of molybdenum in these clusters, which suggests that they are similar to the clusters previously seen by Chen *et al.*[45] during their *in situ* heating experiment (Figure S7). Atomic resolution imaging in that study indicated that these clusters were mainly composed of metal molybdenum nanoparticles, which supports the DFT calculations discussed above. Based on the thermal effects associated with electrical biasing, which will be discussed below, we expect to see clusters similar to those observed by Chen *et al.* when MoS_2 grains are heated.[45] As such, we hypothesize that electrical biasing leads to thermally induced molybdenum and sulfur migration mediated by line defects, which generates long void channels and molybdenum clusters.

Because the Raman modes in MoS_2 red shift due to heating and softening of phonon modes,[46−48] *ex situ* Raman spectroscopy can be used to measure this temperature increase in the suspended material when an electrical bias is applied. In particular, shifts in the position of the A_{1g} mode in MoS_2 are linearly related to the average temperature in the material (Figure S8). In order to estimate the temperature increase present in these suspended devices, Raman peak shifts were first calibrated as a function of temperature below room temperature in a cryostat, which showed trends similar to previously reported values in the literature.[49] Using this relationship, the Raman shifts measured in the A_{1g} mode predicted an upper limit in temperature increase of 180 K in these suspended devices (Figure S8). As even these upper limit values fall within the range of temperature increases previously reported in MoS_2 devices supported by a SiO_2/Si substrate using optothermal Raman techniques,[49] we believe the observations and insights drawn in these suspended devices can be directly translated to MoS_2 devices supported on substrates, as well.

Having suggested that the migration process responsible for void growth is driven by thermally induced motion of sulfur and molybdenum atoms *via* line defects, it is worth exploring how these systems behave after a prolonged period. In Figure 4d, the same region shown in Figure 4a,b is seen after being cycled multiple times from 0 to 5 V at a rate of 100 mV/s. Additionally, a high-resolution image of a nanoribbon fabricated through an identical cycling process is seen in Figure 4e. Following an electrical bias of 10 V, the same region is seen in Figure 4f and displays no discernible structural changes. A video of this process is provided in the SI Video 2. Based on the nearly identical nature of the areas before and after biasing, it is apparent that, in this case, the rate of structural changes diminishes precipitously.

The differences in activation barriers for the migration between molybdenum atoms and sulfur atoms, as discussed previously, may potentially explain the structural stability of this region.[44,45] Namely, it is likely that, with repeated cycles, the line defects mediating this migration process will be continuously shortened through the mechanism suggested by Chen *et al.*[45] In this process, line defects are predicted to slide to voids and molybdenum and sulfur atoms at the edge of these voids migrate into the line defect. This mechanism leads to enlargement of the void and a shortening of the line defect. The shortening of line defects would remove a pathway for the migration of molybdenum atoms and leaves molybdenum-mediated vacancy transport as the most favorable route.[50] Because DFT calculations predict the activation energy for molybdenum atoms through this mechanism to be roughly 3 eV, or twice the activation energy barrier for molybdenum atom migration mediated by line defects, the shortening of line defects would significantly slow down the migration of molybdenum atoms.

https://dx.doi.org/10.1021/acsnano.9b06581
ACS Nano 2020, 14, 1569−1576

Additionally, though high-energy electrons are known to readily create sulfur vacancies, molybdenum atoms tend to be fairly stable and not impact the migration process greatly.[51−53] As such, these resultant structures, such as the narrow ribbons seen in Figure 4e,f, remain stable under electron beam exposure for the small doses used in this study. Our observations suggest that a metastable state is achieved in these samples following several repeated biasing cycles.

CONCLUSIONS

In this study, we present a method for combining electrical biasing with transmission electron microscopy of monolayer MoS_2. We find that voids at the grain boundary of this material play a significant role during electrical biasing. Namely, these neighboring voids coalesce to form long channels likely due to the migration of sulfur and molybdenum atoms. Our results also suggest that the migration of molybdenum atoms serves as the rate-limiting step in this process, which yields a metastable state after prolonged cycling. Through the development of a straightforward methodology for conducting *in situ* electronic measurements on monolayer TMDs and the help of theoretical calculations, we have revealed connections between atomic structure and electronic transport in this system. With this platform, we believe we have created a route for probing a variety of monolayer TMD interfaces in order to better understand and model the complex atomistic interactions at play that give rise to macroscopic properties.

METHODS

Synthesis of MoS_2. Polycrystalline films of monolayer MoS_2 are grown using atmospheric pressure CVD. For this process, 5 mg of MoO_3 (Sigma-Aldrich) powder is evenly spread in an alumina boat and covered by two 1 cm by 1 cm pieces of SiO_2/Si wafer (300 nm oxide thickness) that are placed face down. This boat is then placed within a 1 in. diameter quartz tube and into the center of a furnace. Additionally, 130 mg of sulfur pieces (Alfa-Aesar) is placed in another alumina boat that is placed upstream and outside of the furnace. The tube assembly is then purged for 15 min with argon gas at a flow rate of 13 sccm. The center of the furnace is then heated to 700 °C over a period of 40 min and held at 700 °C for 3 min. During the ramping step, the alumina boat containing the sulfur is moved to a region inside the furnace where the temperature is approximately 150 °C. This is done with the help of a magnet and is performed when the temperature in the center region reaches 575 °C. Following the growth process, the furnace is allowed to cool naturally.

TEM Device Fabrication. A multistep transfer method using polycarbonate stamps is used to suspend material over square TEM apertures. First, a gold electrode structure (75 nm thick) is created through standard e-beam lithography on a SiO_2 substrate. The patterned substrate is coated with a polycarbonate solution (5% polycarbonate to 95% chloroform by weight) at 2000 rpm for 60 s and baked at 120 °C for 1 min. The substrate is placed in DI water for several seconds until the stamp naturally releases from the substrate, lifting off the gold structure. The polycarbonate stamp supporting the gold structure is then removed from the water and allowed to dry naturally in air for several minutes. Once dry, the stamp is carefully placed on top of two strips of polydimethylsulfoxide (PDMS) gel on a glass slide with the gold structure left unsupported and suspended by roughly 1 mm above the glass slide.

Using a micromanipulator, the gold structure is aligned over a TEM window (TEMwindows.com) and brought into contact with the TEM grid. The assembly is gradually heated to 150 °C, which allows the polycarbonate stamp to melt down onto the TEM grid and release from the PDMS support. Once released, the temperature is increased to 170 °C and allowed to bake for 15 min. After being cooled, the structure was put into a chloroform bath for several hours to dissolve the polycarbonate film and then immediately moved to an IPA bath for several minutes to clean off chloroform residue.

This process is repeated for the MoS_2, placing the material over the preprepared TEM window. Samples are left overnight in chloroform and then annealed in a 95% Ar/5% H_2 mixture at 200 °C for 2 h to remove residue prior to TEM imaging. Finally, gold wires are used to connect the electrode pads to the contact points on the TEM mount.

ASSOCIATED CONTENT

Supporting Information

The Supporting Information is available free of charge at https://pubs.acs.org/doi/10.1021/acsnano.9b06581.

Experimental details, TEM images of gold nanoparticles, molybdenum clusters, and void formation, DFT calculations, additional strain maps acquired through geometric phase analysis, and optothermal Raman analysis (PDF)

Video 1: demonstration of the rupture of the nanoribbon connecting two neighboring grains with electrical bias (MOV)

Video 2: demonstration of the stability of the monolayer region with electrical bias following multiple cycles (MOV)

AUTHOR INFORMATION

Corresponding Author

Vinayak P. Dravid − *Department of Materials Science and Engineering, International Institute for Nanotechnology (IIN), and Northwestern University Atomic and Nanoscale Characterization Experimental (NUANCE) Center, Northwestern University, Evanston, Illinois 60208, United States;* orcid.org/0000-0002-6007-3063; Email: v-dravid@northwestern.edu

Authors

Akshay A. Murthy − *Department of Materials Science and Engineering and International Institute for Nanotechnology (IIN), Northwestern University, Evanston, Illinois 60208, United States;* orcid.org/0000-0001-7677-6866

Teodor K. Stanev − *Department of Physics and Astronomy, Northwestern University, Evanston, Illinois 60208, United States*

Roberto dos Reis − *Department of Materials Science and Engineering and Northwestern University Atomic and Nanoscale Characterization Experimental (NUANCE) Center, Northwestern University, Evanston, Illinois 60208, United States*

Shiqiang Hao − *Department of Materials Science and Engineering, Northwestern University, Evanston, Illinois 60208, United States;* orcid.org/0000-0002-7985-4468

Christopher Wolverton − *Department of Materials Science and Engineering, Northwestern University, Evanston, Illinois 60208, United States;* orcid.org/0000-0003-2248-474X

Nathaniel P. Stern − *Department of Physics and Astronomy, Northwestern University, Evanston, Illinois 60208, United States;* orcid.org/0000-0002-8903-3516

Complete contact information is available at: https://pubs.acs.org/10.1021/acsnano.9b06581

Notes

The authors declare no competing financial interest.

A previous version of this paper was uploaded: Murthy, A. A.; Stanev, T. K.; dos Reis, R.; Hao, S.; Wolverton, C.; Stern, N. P.; Dravid, V. P. Direct Visualization of Electric Field Induced Structural Dynamics in Monolayer Transition Metal Dichalcogenides; https://arxiv.org/abs/1910.02879.

https://dx.doi.org/10.1021/acsnano.9b06581
ACS Nano 2020, 14, 1569−1576

ACKNOWLEDGMENTS

This material is based upon work supported by the National Science Foundation under Grant Nos. DMR-1507810 and DMR-1929356. This work made use of the EPIC, Keck-II, and SPID facilities of Northwestern University's NUANCE Center, which has received support from the Soft and Hybrid Nanotechnology Experimental (SHyNE) Resource (NSF ECCS-1542205); the MRSEC program (NSF DMR-1720319) at the Materials Research Center; the International Institute for Nanotechnology (IIN); the Keck Foundation; and the State of Illinois, through the IIN. This work also made use of a cryostat platform for confocal microscopy (AttoCube AttoDry 2100, supported by Office of Naval Research N00014-18-1-2131). A.A.M. gratefully acknowledges support from the Ryan Fellowship and the IIN at Northwestern University. T.K.S. was supported by the Office of Naval Research (N00014-16-1-3055). DFT calculations were conducted using the high performance computational resources at Northwestern University and supported by the Department of Energy, Office of Science, Basic Energy Sciences under grant DE-SC0014520. The authors thank Dr. Anahita Pakzad and Dr. Benjamin Miller from Gatan, Inc, Pleasanton, CA, for the valuable feedback on the usage of K3-IS direct detector.

REFERENCES

(1) Zhou, W.; Zou, X.; Najmaei, S.; Liu, Z.; Shi, Y.; Kong, J.; Lou, J.; Ajayan, P. M.; Yakobson, B. I.; Idrobo, J. C. Intrinsic Structural Defects in Monolayer Molybdenum Disulfide. *Nano Lett.* **2013**, *13*, 2615−2622.

(2) McDonnell, S.; Addou, R.; Buie, C.; Wallace, R. M.; Hinkle, C. L. Defect-Dominated Doping and Contact Resistance in MoS2. *ACS Nano* **2014**, *8*, 2880−2888.

(3) Tongay, S.; Suh, J.; Ataca, C.; Fan, W.; Luce, A.; Kang, J. S.; Liu, J.; Ko, C.; Raghunathanan, R.; Zhou, J.; Ogletree, F.; Li, J.; Grossman, J. C.; Wu, J. Defects Activated Photoluminescence in Two-Dimensional Semiconductors: Interplay Between Bound, Charged, and Free Excitons. *Sci. Rep.* **2013**, *3*, 2657.

(4) Nan, H.; Wang, Z.; Wang, W.; Liang, Z.; Lu, Y.; Chen, Q.; He, D.; Tan, P.; Miao, F.; Wang, X.; Wang, J.; Ni, Z. Strong Photoluminescence Enhancement of MoS2 through Defect Engineering and Oxygen Bonding. *ACS Nano* **2014**, *8*, 5738−5745.

(5) Li, H.; Tsai, C.; Koh, A. L.; Cai, L.; Contryman, A. W.; Fragapane, A. H.; Zhao, J.; Han, H. S.; Manoharan, H. C.; Abild-Pedersen, F.; Norskov, J. K.; Zheng, X. Activating and Optimizing MoS2 Basal Planes for Hydrogen Evolution through the Formation Of Strained Sulphur Vacancies. *Nat. Mater.* **2016**, *15*, 48−53.

(6) Ye, G.; Gong, Y.; Lin, J.; Li, B.; He, Y.; Pantelides, S. T.; Zhou, W.; Vajtai, R.; Ajayan, P. M. Defects Engineered Monolayer MoS2 for Improved Hydrogen Evolution Reaction. *Nano Lett.* **2016**, *16*, 1097−1103.

(7) van der Zande, A. M.; Huang, P. Y.; Chenet, D. A.; Berkelbach, T. C.; You, Y.; Lee, G. H.; Heinz, T. F.; Reichman, D. R.; Muller, D. A.; Hone, J. C. Grains and Grain Boundaries in Highly Crystalline Monolayer Molybdenum Disulphide. *Nat. Mater.* **2013**, *12*, 554−561.

(8) Zou, X.; Liu, Y.; Yakobson, B. I. Predicting Dislocations and Grain Boundaries in Two-Dimensional Metal-Disulfides from the First Principles. *Nano Lett.* **2013**, *13*, 253−258.

(9) Liu, X. L.; Balla, I.; Bergeron, H.; Hersam, M. C. Point Defects and Grain Boundaries in Rotationally Commensurate MoS2 On Epitaxial Graphene. *J. Phys. Chem. C* **2016**, *120*, 20798−20805.

(10) Huang, Y. L.; Chen, Y.; Zhang, W.; Quek, S. Y.; Chen, C. H.; Li, L. J.; Hsu, W. T.; Chang, W. H.; Zheng, Y. J.; Chen, W.; Wee, A. T. Bandgap Tunability at Single-Layer Molybdenum Disulphide Grain Boundaries. *Nat. Commun.* **2015**, *6*, 6298.

(11) Rong, Y.; Sheng, Y.; Pacios, M.; Wang, X.; He, Z.; Bhaskaran, H.; Warner, J. H. Electroluminescence Dynamics across Grain Boundary Regions of Monolayer Tungsten Disulfide. *ACS Nano* **2016**, *10*, 1093−1100.

(12) Sangwan, V. K.; Jariwala, D.; Kim, I. S.; Chen, K. S.; Marks, T. J.; Lauhon, L. J.; Hersam, M. C. Gate-Tunable Memristive Phenomena Mediated by Grain Boundaries in Single-Layer Mos2. *Nat. Nanotechnol.* **2015**, *10*, 403−406.

(13) Sangwan, V. K.; Lee, H. S.; Bergeron, H.; Balla, I.; Beck, M. E.; Chen, K. S.; Hersam, M. C. Multi-Terminal Memtransistors from Polycrystalline Monolayer Molybdenum Disulfide. *Nature* **2018**, *554*, 500−504.

(14) Yasaei, P.; Murthy, A. A.; Xu, Y.; Dos Reis, R.; Shekhawat, G. S.; Dravid, V. P. Spatial Mapping of Hot-Spots at Lateral Heterogeneities in Monolayer Transition Metal Dichalcogenides. *Adv. Mater.* **2019**, *31*, 1808244.

(15) Rong, Y.; He, K.; Pacios, M.; Robertson, A. W.; Bhaskaran, H.; Warner, J. H. Controlled Preferential Oxidation of Grain Boundaries in Monolayer Tungsten Disulfide for Direct Optical Imaging. *ACS Nano* **2015**, *9*, 3695−3703.

(16) Gao, J.; Li, B.; Tan, J.; Chow, P.; Lu, T. M.; Koratkar, N. Aging of Transition Metal Dichalcogenide Monolayers. *ACS Nano* **2016**, *10*, 2628−2635.

(17) Huang, J. Y.; Zhong, L.; Wang, C. M.; Sullivan, J. P.; Xu, W.; Zhang, L. Q.; Mao, S. X.; Hudak, N. S.; Liu, X. H.; Subramanian, A.; Fan, H.; Qi, L.; Kushima, A.; Li, J. *In Situ* Observation of the Electrochemical Lithiation of a Single SnO2 Nanowire Electrode. *Science* **2010**, *330*, 1515−1520.

(18) Liu, X. H.; Wang, J. W.; Huang, S.; Fan, F.; Huang, X.; Liu, Y.; Krylyuk, S.; Yoo, J.; Dayeh, S. A.; Davydov, A. V.; Mao, S. X.; Picraux, S. T.; Zhang, S.; Li, J.; Zhu, T.; Huang, J. Y. *In Situ* Atomic-Scale Imaging of Electrochemical Lithiation in Silicon. *Nat. Nanotechnol.* **2012**, *7*, 749−756.

(19) Luo, L.; Wu, J.; Luo, J.; Huang, J.; Dravid, V. P. Dynamics of Electrochemical Lithiation/Delithiation of Graphene-Encapsulated Silicon Nanoparticles Studied by *In-Situ* TEM. *Sci. Rep.* **2015**, *4*, 3863.

(20) Liu, Q.; Sun, J.; Lv, H.; Long, S.; Yin, K.; Wan, N.; Li, Y.; Sun, L.; Liu, M. Real-Time Observation on Dynamic Growth/Dissolution of Conductive Filaments in Oxide-Electrolyte-Based ReRAM. *Adv. Mater.* **2012**, *24*, 1844−1849.

(21) Yang, Y.; Gao, P.; Gaba, S.; Chang, T.; Pan, X.; Lu, W. Observation of Conducting Filament Growth in Nanoscale Resistive Memories. *Nat. Commun.* **2012**, *3*, 732.

(22) Kwon, D. H.; Kim, K. M.; Jang, J. H.; Jeon, J. M.; Lee, M. H.; Kim, G. H.; Li, X. S.; Park, G. S.; Lee, B.; Han, S.; Kim, M.; Hwang, C. S. Atomic Structure of Conducting Nanofilaments in TiO2 Resistive Switching Memory. *Nat. Nanotechnol.* **2010**, *5*, 148−153.

(23) Fan, Y.; Robertson, A. W.; Zhou, Y.; Chen, Q.; Zhang, X.; Browning, N. D.; Zheng, H.; Rummeli, M. H.; Warner, J. H. Electrical Breakdown of Suspended Mono- and Few-Layer Tungsten Disulfide *via* Sulfur Depletion Identified by *In Situ* Atomic Imaging. *ACS Nano* **2017**, *11*, 9435−9444.

(24) Fan, Y.; Robertson, A. W.; Zhang, X.; Tweedie, M.; Zhou, Y.; Rummeli, M. H.; Zheng, H.; Warner, J. H. Negative Electro-Conductance in Suspended 2D WS2 Nanoscale Devices. *ACS Appl. Mater. Interfaces* **2016**, *8*, 32963−32970.

(25) Murthy, A. A.; Stanev, T. K.; Cain, J. D.; Hao, S.; LaMountain, T.; Kim, S.; Speiser, N.; Watanabe, K.; Taniguchi, T.; Wolverton, C.; Stern, N. P.; Dravid, V. P. Intrinsic Transport in 2D Heterostructures Mediated through h-BN Tunneling Contacts. *Nano Lett.* **2018**, *18*, 2990−2998.

(26) Chae, W. H.; Cain, J. D.; Hanson, E. D.; Murthy, A. A.; Dravid, V. P. Substrate-Induced Strain and Charge Doping in CVD-Grown Monolayer MoS_2. *Appl. Phys. Lett.* **2017**, *111*, 143106.

(27) Hakkinen, H. The Gold-Sulfur Interface at the Nanoscale. *Nat. Chem.* **2012**, *4*, 443−55.

(28) Gong, C.; Huang, C.; Miller, J.; Cheng, L.; Hao, Y.; Cobden, D.; Kim, J.; Ruoff, R. S.; Wallace, R. M.; Cho, K.; et al. Metal Contacts on Physical Vapor Deposited Monolayer MoS2. *ACS Nano* **2013**, *7*, 11350−11357.

https://dx.doi.org/10.1021/acsnano.9b06581
ACS Nano 2020, 14, 1569−1576

(29) Scheuschner, N.; Ochedowski, O.; Kaulitz, A. M.; Gillen, R.; Schleberger, M.; Maultzsch, J. Photoluminescence of Freestanding Single- and Few-Layer MoS2. *Phys. Rev. B: Condens. Matter Mater. Phys.* **2014**, *89*, 125406.
(30) O'Brien, M.; Scheuschner, N.; Maultzsch, J.; Duesberg, G. S.; McEvoy, N. Raman Spectroscopy of Suspended MoS2. *Phys. Status Solidi B* **2017**, *254*, 1700218.
(31) Sorensen, S. G.; Fuchtbauer, H. G.; Tuxen, A. K.; Walton, A. S.; Lauritsen, J. V. Structure and Electronic Properties of *In Situ* Synthesized Single-Layer MoS2 on a Gold Surface. *ACS Nano* **2014**, *8*, 6788−6796.
(32) Mak, K. F.; Lee, C.; Hone, J.; Shan, J.; Heinz, T. F. Atomically Thin MoS2: A New Direct-Gap Semiconductor. *Phys. Rev. Lett.* **2010**, *105*, 136805.
(33) Li, Y.; Wu, D.; Zhou, Z.; Cabrera, C. R.; Chen, Z. Enhanced Li Adsorption and Diffusion on MoS2 Zigzag Nanoribbons by Edge Effects: A Computational Study. *J. Phys. Chem. Lett.* **2012**, *3*, 2221−2227.
(34) Li, Y.; Cain, J. D.; Hanson, E. D.; Murthy, A. A.; Hao, S.; Shi, F.; Li, Q.; Wolverton, C.; Chen, X.; Dravid, V. P. Au@ MoS2 Core−Shell Heterostructures with Strong Light−Matter Interactions. *Nano Lett.* **2016**, *16*, 7696−7702.
(35) Li, Y.; DiStefano, J. G.; Murthy, A. A.; Cain, J. D.; Hanson, E. D.; Li, Q.; Castro, F. C.; Chen, X.; Dravid, V. P. Superior Plasmonic Photodetectors Based on Au@MoS2 Core-Shell Heterostructures. *ACS Nano* **2017**, *11*, 10321−10329.
(36) Gong, C.; Colombo, L.; Wallace, R. M.; Cho, K. The Unusual Mechanism of Partial Fermi Level Pinning at Metal-MoS2 Interfaces. *Nano Lett.* **2014**, *14*, 1714−1720.
(37) Rahaman, M.; Rodriguez, R. D.; Plechinger, G.; Moras, S.; Schuller, C.; Korn, T.; Zahn, D. R. T. Highly Localized Strain in a MoS2/Au Heterostructure Revealed by Tip-Enhanced Raman Spectroscopy. *Nano Lett.* **2017**, *17*, 6027−6033.
(38) Li, S. L.; Wakabayashi, K.; Xu, Y.; Nakaharai, S.; Komatsu, K.; Li, W. W.; Lin, Y. F.; Aparecido-Ferreira, A.; Tsukagoshi, K. Thickness-Dependent Interfacial Coulomb Scattering in Atomically Thin Field-Effect Transistors. *Nano Lett.* **2013**, *13*, 3546−3552.
(39) Liu, H.; Neal, A. T.; Ye, P. D. Channel Length Scaling of MoS2MOSFETs. *ACS Nano* **2012**, *6*, 8563−8569.
(40) Elibol, K.; Susi, T.; O'Brien, M.; Bayer, B. C.; Pennycook, T. J.; McEvoy, N.; Duesberg, G. S.; Meyer, J. C.; Kotakoski, J. Grain Boundary-Mediated Nanopores in Molybdenum Disulfide Grown by Chemical Vapor Deposition. *Nanoscale* **2017**, *9*, 1591−1598.
(41) Ly, T. H.; Perello, D. J.; Zhao, J.; Deng, Q.; Kim, H.; Han, G. H.; Chae, S. H.; Jeong, H. Y.; Lee, Y. H. Misorientation-Angle-Dependent Electrical Transport Across Molybdenum Disulfide Grain Boundaries. *Nat. Commun.* **2016**, *7*, 10426.
(42) Hÿtch, M. J.; Snoeck, E.; Kilaas, R. Quantitative Measurement of Displacement and Strain Fields from HREM Micrographs. *Ultramicroscopy* **1998**, *74*, 131−146.
(43) Liu, Y.; Guo, J.; Zhu, E.; Liao, L.; Lee, S. J.; Ding, M.; Shakir, I.; Gambin, V.; Huang, Y.; Duan, X. Approaching the Schottky-Mott Limit in van der Waals Metal-Semiconductor Junctions. *Nature* **2018**, *557*, 696−700.
(44) Yu, Z. G.; Zhang, Y. W.; Yakobson, B. I. An Anomalous Formation Pathway for Dislocation-Sulfur Vacancy Complexes in Polycrystalline Monolayer MoS2. *Nano Lett.* **2015**, *15*, 6855−6861.
(45) Chen, Q.; Li, H.; Zhou, S.; Xu, W.; Chen, J.; Sawada, H.; Allen, C. S.; Kirkland, A. I.; Grossman, J. C.; Warner, J. H. Ultralong 1D Vacancy Channels for Rapid Atomic Migration during 2D Void Formation in Monolayer MoS2. *ACS Nano* **2018**, *12*, 7721−7730.
(46) Taube, A.; Judek, J.; Lapinska, A.; Zdrojek, M. Temperature-Dependent Thermal Properties of Supported MoS2Monolayers. *ACS Appl. Mater. Interfaces* **2015**, *7*, 5061−5065.
(47) Judek, J.; Gertych, A. P.; Swiniarski, M.; Lapinska, A.; Duzynska, A.; Zdrojek, M. High Accuracy Determination of the Thermal Properties Of Supported 2D Materials. *Sci. Rep.* **2015**, *5*, 12422.
(48) Zhang, X.; Sun, D.; Li, Y.; Lee, G. H.; Cui, X.; Chenet, D.; You, Y.; Heinz, T. F.; Hone, J. C. Measurement of Lateral and Interfacial Thermal Conductivity of Single- and Bilayer MoS2 and MoSe2 Using Refined Optothermal Raman Technique. *ACS Appl. Mater. Interfaces* **2015**, *7*, 25923−25929.
(49) Yalon, E.; McClellan, C. J.; Smithe, K. K. H.; Munoz Rojo, M.; Xu, R. L.; Suryavanshi, S. V.; Gabourie, A. J.; Neumann, C. M.; Xiong, F.; Farimani, A. B.; Pop, E. Energy Dissipation in Monolayer MoS2 Electronics. *Nano Lett.* **2017**, *17*, 3429−3433.
(50) Hong, J.; Pan, Y.; Hu, Z.; Lv, D.; Jin, C.; Ji, W.; Yuan, J.; Zhang, Z. Direct Imaging of Kinetic Pathways of Atomic Diffusion in Monolayer Molybdenum Disulfide. *Nano Lett.* **2017**, *17*, 3383−3390.
(51) Zan, R.; Ramasse, Q. M.; Jalil, R.; Georgiou, T.; Bangert, U.; Novoselov, K. S. Control of Radiation Damage in MoS2 by Graphene Encapsulation. *ACS Nano* **2013**, *7*, 10167−10174.
(52) KC, S.; Longo, R. C; Addou, R.; Wallace, R. M; Cho, K. Impact of Intrinsic Atomic Defects on the Electronic Structure of MoS2Monolayers. *Nanotechnology* **2014**, *25*, 375703.
(53) Lin, Y. C.; Dumcenco, D. O.; Komsa, H. P.; Niimi, Y.; Krasheninnikov, A. V.; Huang, Y. S.; Suenaga, K. Properties of Individual Dopant Atoms in Single-Layer MoS2: Atomic Structure, Migration, and Enhanced Reactivity. *Adv. Mater.* **2014**, *26*, 2857−2861.

https://dx.doi.org/10.1021/acsnano.9b06581
ACS Nano 2020, 14, 1569−1576